MECH0020 Individual Project

2018/19

Student:	Adhiphu Sajjaphanroj
Project Title:	Mechanics of Creased Membrane for Space Antennas
Supervisor:	Dr. Federico Bosi

Word count: 7091 words

Declaration

I, Adhiphu Sajjaphanroj, confirm that the work presented in this report is my own. Where information has been derived from other sources, I confirm that this has been indicated in the report.

Signed

Date   26/04/2019

BLANK PAGE

Abstract

Almost a hundred space launch attempts were made in 2017, carrying over 460 satellites, a far cry from less than 200 satellites only 5 years prior. However, also growing is the interest in launch vehicles with small payloads despite the designs of space antennas increasing in size. Extensive studies have been conducted on many aspects of the designs themselves – from materials to folding patterns of deployable antennas – but little interest exists in investigating the tensile force required to maintain the surface accuracy of an aperture to be within the permissible tolerance.

Although several papers have been written on the deformation of creased structures, these often carry assumptions on the shape of the creases. Conversely, researches which defined the effects of creases on structures failed to cover the relationship of forces and displacements. This study aimed to define the surface accuracy of a creased membrane as a function of the tensile force applied without undue assumptions, as well as exploring the methods to model membranes with multiple-creases. As such, a function was defined by applying the Castigliano's second theorem to a 2D beam. The quadratic mean (RMS), a measure of surface accuracy, of vertical displacements along the deflected beam with respect to the desired flat position can subsequently be calculated from the deflection obtained.

The defined function is sufficiently accurate in specifying the force required to achieve the desired surface accuracy of the membrane with respect to the tolerance of a space antenna that operates within the Ku-band. On the other hand, different methods were applied to create the 3D model of a membrane with multiple creases, but the responses obtained were not as expected, as the middle section of the model failed to react to the load applied. However, the results veered to be in line with what was expected upon the addition of a support under the middle section.

BLANK PAGE

Acknowledgement

BLANK PAGE

Contents

BLANK PAGE

Nomenclature

Abbreviation	Units	Description
E	Pa	Young's modulus
I	m^4	Second moment of inertia
M_0	N m	Bending moment
M_s	N m	Spring moment
k	N m deg^{-1}	Rotational stiffness
α	deg	Neutral angle
U_m	N m	Strain energy
D_y	N	Dummy force
$δ_y$	m	Vertical deflection
RMS	m	Root-mean-square of the vertical deflection from the flat-point datum line
ν	-	Poisson ratio
	-	Global cartesian coordinates system used throughout this paper.

List of figures

List of tables

BLANK PAGE

1. Introduction

1.1 Project Background & Problem

Antennas are transducers capable of converting electromagnetic waves into electrical current, and vice versa. Utilised for the transmission of information over long distances, an antenna can either be for receiving, transmitting data, or both. These devices form the major parts of satellites systems for a multitude of space missions - from telecommunication to deep-space exploration - and have become one of the most important technologies that facilitate the everyday life of most communities, from enabling basic communications to gathering research data.

In earth-orbit, each satellite system can be categorised into three types: Fixed Satellite Communications, Direct Satellite Broadcasting, and Mobile Satellite Communications. Each antenna is designed to cater for a specific band of radio frequency, although some devices are capable of operating in multiple frequency bands. Ku-band (12-18 GHz), in particular, is the operational frequency of most Direct Satellite Broadcasting devices responsible for satellite televisions with its short wavelength that has enabled the usage of compact household satellite dishes. Moreover, an antenna's construction can be either planar or parabolic, and further classifiable into three main design types, including the Len, Phased Array, and Reflector Antennas.

(a) Folded   *(b) Deployed, plan view*
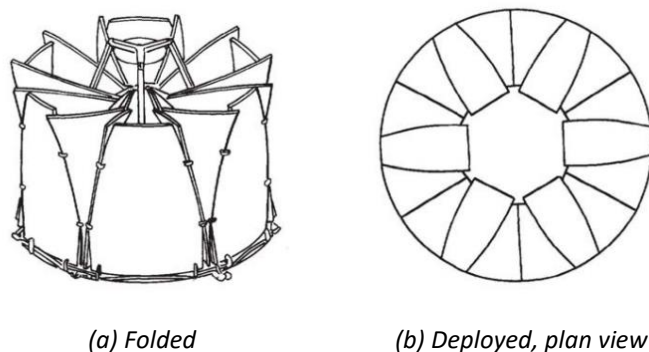
Figure 1 TRW Advanced Sunflower Precision antenna[1]

However, regardless of the type and operational frequency, the performance of an antenna is determined by its "Gain", that is the measure of its ability to amplify the output signal relative to the amplitude of the input. Unlike receive-only antennas that are

exposed to incoming waves with shifting directions - such as those in mobile phones - that require low gains, space antennas are designed to achieve the highest gain possible. Subsequently, as gain is directly proportional to an antenna's Effective Aperture Area, larger antennas are preferred. Consequently, with respect to the high costs of launching and in-space assembly, the status quo has been revolving around the investigation of self-deployable antenna designs which will be able to achieve large aperture area with minimal mass and low stowage volume. Early concepts such as the TRW Advanced Sunflower Precision Antenna (see *Figure* 1) was studied by Russell et al.[2] of NASA Langley Research Centre in 1980 and it attained an aperture area of more than 7 m^2 with the mass of 67.6 kg. In comparison, the Synthetic Aperture Radar (SAR) satellite RADARSAT-2 launched on 14-Dec-2007 has the area of 22 m^2 and weighting in at almost 850 kg.[3] The 75% reduction in areal density such as this is indeed the main reason behind the sustained interest on this subject.

Figure 2 A creased membrane prototype [4]

Since then, multiple deployment and stowage mechanisms have been explored and "Membrane" antennas were developed with new material requirements. That is, although the aperture materials must be flexible enough to be folded or rolled-up to reduce the required payload volume, they must also be able to withstand exposure to space radiation, and the effect of thermal distortion in orbit that can range from 430°C to -250°C. One of the most important criteria, however, is with regards to the ability of the material and tensioning mechanism, or otherwise, to maintain the adequate level of surface flatness as it is directly related to the directional accuracy of the antenna. Specifically, the surface accuracy should at least be in the same order as 1/30 of the respective free-space wavelength of the operational frequency.[5] For example, the acceptable tolerance for Ku-band antennas is approximately ±0.1mm.

As such, whilst the departure from solid aperture construction has allowed for the development of engineered creases that enable elaborate folding patterns, such as the prototype developed by Lee and Pellegrino[4] in *Figure 2*, it has also raised the question of how these creases – which did not exist on previous antenna designs - will affect the flatness of the membranes. Even more importantly perhaps: how to achieve the flattest surface possible upon the deployment of antennas.

1.2 Literature Review

(a) Multiple-creases membrane with corner forces   *(b) Simplified model of the creases*
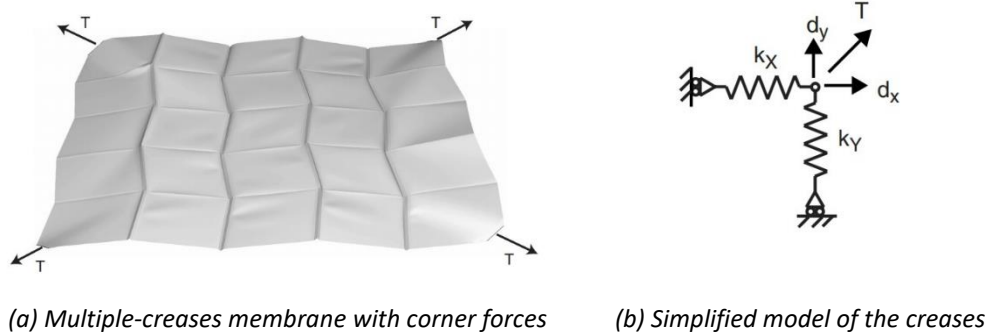
Figure 3 Models investigated by Papa and Pellegrino[9]

Many researches have been carried out to investigate creases, as evident by the paper written by Wang et al.[6] which investigated the relationship between creases and wrinkles on a membrane, or a similar study conducted by Xiao et al.[7] from Shanghai Jiaotong University on the same characteristics but specifically for space inflatable antennas. Nevertheless, by its own definition, wrinkles are "the elastic response of a membrane due to localised buckling in compressed area[6]", and these studies did not cover the response of a creased structure in tension. Tension being the state in which a stretched membrane antenna will be in, fortunately, in recent years more efforts have been invested into studying the mechanical responses of creased membranes under such condition, and where it does not concern wrinkles. A study conducted by Lechenault at al.[8], for instance, investigated the characteristics of the creases themselves. The result of the research provided the information concerning whether a specimen being pulled will response overwhelmingly in increased creased angle, or panel bending, yet it does not delve into surface accuracy. Nevertheless, in doing so, the paper confirmed the hinge-like behaviour of the creases and that a torsional elasticity could be incorporated to represent the

increase in stiffness in the area surrounding a crease. A previous paper authored by Papa and Pellegrino[9] in 2008 made progress in investigating the load-displacement relationship of a multiple square-creased membrane subjected to diagonal tensile forces but the study treated entire sections of the membrane as single springs with constant stiffness, as shown in *Figure 3*. Furthermore, both the analytical and numerical model investigated were focused on defining the horizontal displacements, and not necessarily the flatness of the surface.

However, despite the additional studies which had been made on the mechanics and responses of creased sheets, or membranes, researches which look at characteristics of the membrane, specifically for deployable space antennas, in tension and for the purpose of defining the relationship between the load applied and the surface accuracy of the membrane remain scarce. Moreover, few relevant researches conventionally focus on articulating one aspect of modelling or mechanics of responses: creased angle, membrane deflection, stress distribution, etc. rather than combining the solutions available. Additionally, since the paper published in 2008 previously mentioned[9], no further major advancement was conducted to establish an analytical solution for the load-displacement relationship. However, following the ways to accurately analyse the deflection of a beam, one can arrive at the study on deflections of a cantilever beam by Mutyalarao et al.[10] which built on the flexural theory, and moment-curvature relationship. It goes on to describe the deformation of a cantilever beam subjected to a concentrated load at the unsupported end. On the contrary, the numerical analysis of creased structure has been receiving more focus – although the number of studies remains limited. In 2018, Dharmadasa et al.[11] released a study on the numerical analysis of a creased membrane made from Kapton film, a material widely used for the deployable space structures (see *section 1.4*). The paper modelled the crease as a torsional spring with the constants experimentally obtained. Furthermore, the study has also obtained the "neutral angle", or the opening angle of the creased membrane after a prolonged period of undisturbed relaxation, of the creased Kapton film membrane, paving the ways to model the initial position for future studies, including this one. Moreover, the paper also verified the symmetry condition of a thin creased film via comparing the analytically obtained deformed shape of a 2D model to the 3D models generated with ABAQUS. In modelling the creased-membranes on ABAQUS themselves, Dharmadasa et al. relied on an earlier

paper which involved the method to correctly incorporate the additional rotational elasticity onto the membrane.

This paper will attempt to build on the products of past studies, including but not limited to the researches mentioned prior, to achieve the project objective with respect to the specified scope.

1.3 Project Scope & Objective

In the attempt to address the loophole of the current field of study concerning the relationship between tensile load and the surface accuracy of a deployable space antenna membrane previously put forward, the objective of this project is to understand the relationship between the measure of surface accuracy and the tensile force applied horizontally to one end of the membrane. The former refers to quadratic means (RMS) taken of the vertical deflection of a membrane when subjected to load with respect to the relative datum line that represents the desired horizontally flat position. The relationship will enable the prediction of forces required to obtain the appropriate level of membrane flatness, and therefore the required gain.

Subsequently, validation of the solution will be carried out using 2 numerical models created via the Finite Element Analysis (FEA) software ABAQUS: an exact 2D replication of the analytical model, and the 3D equivalent. The two models which theoretically represent the same specimen will also provide the basis for verifying the symmetry assumption conventionally taken in previous studies.

Furthermore, building on past methods, this paper will attempt to create a membrane with multiple-creases taking into account the finite rotational elasticity of the creases. Not to mention the very limited number of papers available on numerically modeling membrane with more than one creases, past models have either recreated the crease by "welding" planar membranes together or connecting them with a "hinge"; both proven to inaccurate by the study by Lechenault et al.[8] as previously mentioned.

1.4 Material Selection

While one of the objectives of the project is to find a general equation to predict the surface accuracy of the membrane as a function of the variable tensile force acting on the membrane on deployment, a variation of the Polyimide film (PET) called Kapton and its characteristics was used as the reference material properties in validating and calculating the results from the numerical, analytical analysis. Although there are two types of polymerous materials commonly used in the design of space structures, and these are Polyester (PI), and PET films of varying dimensions, the latter was chosen due to its lasting incorporation into many designs of deployable antennas.

Earlier models used intrinsically (electrically) conductive material such as molybdenum wire mesh, however, polymer films coated with reflective metals such as copper, or aluminum, have gained in popularity due to its superior flexibility and ease of manufacturing. Of the different types of polymer, as early as the 1990s, Kapton (PET) was used as the substrate for solar cells of the Inflatable Tous Solar Array (ITSAT) programme. More recently, researches have been conducted to invent materials specifically for space antenna: the European Space Agency (ESA) along with the Swiss Contraves Division have developed a Shape Memory Polymer impregnated Kevlar Fibres usable intended for inflation-rigidisation deployment, whereas the material rigidises within 6 hours after exposure to solar radiation. Unfortunately, with respect to the constraint of public supply availability which may restrict the ability for the results obtained in this study to be validated with experimental results in the future, properties of plain non-coated films were used instead of metal-coated film typically utilised in actual designs.

2. Analytical Solution

2.1 Structure Simplification

Considering the scarcity of preceding materials on this subject, the analytical calculation was conducted on simplified mass-less beam structures to represent membranes with a single crease (see *Figure 5*). These beam models are viable when the symmetry conditions of a membrane is considered. That is, for a membrane in which the crease was located at exactly halfway through the length, perpendicular to the longitudinal axis, and spanned across the entire width of the membrane as shown in *Figure 5* only one half of the membrane was deemed necessary to be investigated because the bilateral symmetry condition applies, and the structural responses are expected to be mirrored on the other side. Additionally, the transverse symmetry, which in this context refers to the identicality of the cross-sections of the membrane that lie on the planes perpendicular to the yz-plane, means that the use of 2D models was also justified. Taking the symmetry assumptions also provide the additional advantage of reducing the computing power, and time, required in obtaining the numerical solutions.

The following two sections describe the specific assumptions employed with regards to the bilateral symmetry, as well as the adjustments made to replicate the effect of the crease. Further investigation was made with regards to the 2D simplification and discussed in more detail in section 4.1.

2.1.1 Assumptions and Boundary Conditions.

Firstly, the conventional assumptions of the pure bending theory were applied to maintain the suitability of the Castigliano's second theorem. The main assumptions being that the material is homogeneous and isotropic, plane cross-sections remain plane before and after bending, every cross-section in the beam is symmetrical about the plane of bending, the flexural stiffness is constant, and the elastic limit is not exceeded. Secondly, in order to best simulate the response, multiple combinations of boundary conditions were investigated to identify the most accurate representation of the creased membrane.

(a) Structure 1   (b) Structure 2
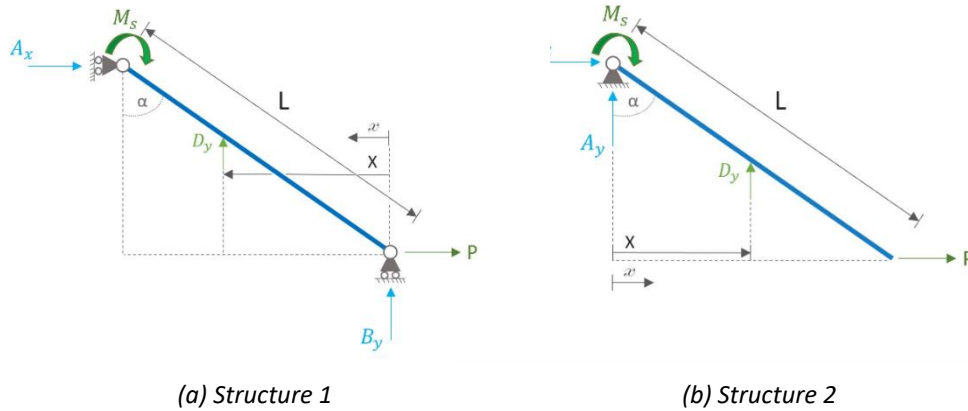
Figure 4 Beam model used for the analytical solution.
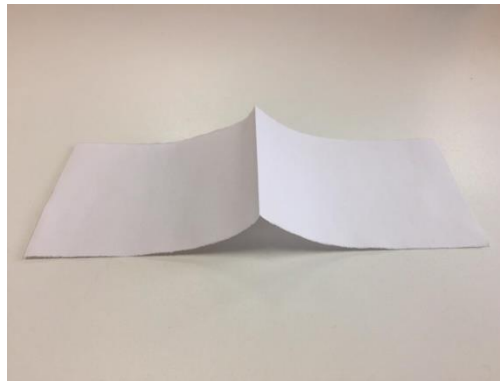
Figure 5 A simple single-creased membrane

The first structure (*Figure 4a*) has a roller support on its right end to simulate the constraint in vertical displacements imposed by a membrane's attachment to its tensioning structure. The opposite end is buttressed by another roller support facing the juxtaposing direction as a necessary symmetry boundary, whilst allowing for vertical displacements as the membrane becomes flatter due to the tensioning force. Alternatively, the second structure investigated (*Figure 4b*) only has one pinned support on the left-end and a free end on the other with only the force applied.

In both cases, the force itself is applied as a point load in the positive x-axis direction, as a result of the models being analysed as a 2D structure – albeit the dimensions of the cross-section was taken into account. The 2D simplification, and subsequently the point load, is justifiable by the fact that one of the aims in the development of different tensioning systems is to achieve a uniform stress distribution along the edge (width) of the membrane.[12] As such, in addition to the lengthwise geometric symmetry of the

membrane, it was also possible to sum-up the response of the actual structure into a 2D model by defining the magnitude of the point load as a product of the uniformly distributed "force/unit length" and the width of the membrane for the subsequent analyses of the 3D models.

2.1.2 Simulating the Crease

The measure of a structure's resistance to bending, or bending stiffness, is called the flexural rigidity (EI). Mathematically, it is defined as the product of the Young's modulus of the material and its second moment of inertia (I). For a structure with a rectangular cross-section:

$$I = \frac{bh^3}{12}$$

Where b is the width, and h is the depth of the cross-section. Thus, EI is directly proportional to the depth of the structure. As a form of plastic deformation, the introduction of creases into a membrane permanently increases the ultimate depth of the membrane, and subsequently its bending stiffness. However, the exact change in EI is dependent on the uniformity, shape, and sizes of the crease amongst other factors and it is beyond the scope of this project. Hence, for the purpose of this analysis, and with regards to the assumption of constant flexural rigidity, a torsional spring was attached to the left end of both structures to signify the effect of the crease.

As illustrated in *Figure 4*, M_s represents the spring moment in the clockwise direction opposing the expected direction of motion of the beam.

In which $$M_s = k(\theta - \alpha)$$

Where k is the hinge stiffness, θ is the counterclockwise angle of the beam relative to the y-axis from the origin, and α is half the neutral angle of a creased membrane of the same material after a period of undisturbed post-crease relaxation. At time $t = 0, \alpha = \theta$.

For a Kapton film membrane of 50 μm thickness, Dharmadasa et al.[11] experimentally obtained the stiffness k, and the angle α, to be at $0.0006 * b$ N m deg^{-1} and $0.5 * 89$ deg. respectively.

2.2 Castigliano's Second Theorem

One of the methods for deriving small displacements within a linearly elastic structure is the theorem developed by Carlo Alberto Castigliano which relates displacements in a given direction to the partial derivative of the strain energy with respect to the force acting in the same direction. Mathematically, this can be represented as below

$$\delta_y = \frac{\partial U_m}{\partial D_y}$$

Where U_m is the total strain energy, and D_y is the dummy force added onto the structures, as shown in *Figure 4*, in order to facilitate the calculation of the vertical deflection δ_y with respect to the horizontal distance X along the beam. On the other hand, the lower-case x refers to the variation of the bending moment with respect to the beam length specific to each constant location of D_y.

For both structures,

$$U_M = \int_{x=0}^{x=L\sin\alpha} \frac{M_0^2}{2EI}\, dx + \frac{M_s^2}{2k}$$

With the second term representing the additional strain energy as a result of the torsional spring and k represents the spring stiffness, as per the Hooke's law.

2.2.1 Structure 1

Assuming a static beam, the torsional spring moment M_s was found to be as below.

$$M_s = -D_y X + PL\cos\alpha$$

Where X is extending from the right-end of the structure. Following the standard beam analysis procedures, the model was divided into two sections and the bending moment was calculated for each.

For the section $\qquad\qquad\qquad\qquad\qquad 0 \leq x < X$

The bending moment is $\qquad\qquad M_{0,1} = \frac{Px}{\tan\alpha} - D_y x + D_y X - PL\cos\alpha$

For the second section $\qquad\qquad\qquad\qquad X \leq x < L\sin\alpha$

The bending moment is
$$M_{0,2} = \frac{Px}{\tan\alpha} - PL\cos\alpha$$

Therefore, separating $\frac{\partial U_m}{\partial D_y}$ into three parts, the vertical deflection in the first section can be obtained as follow.

$$\frac{\partial U_{m,1}}{\partial D_y} = \frac{\partial U_{m,1}}{\partial M_{0,1}}\left(\frac{\partial M_{0,1}}{\partial D_y}\right)$$

$$= \frac{1}{EI}\int_0^X \left[M_{0,1}\cdot(X-x)\right]dx$$

$$= \frac{1}{EI}\left(\frac{PX^3}{6\tan\alpha} - \frac{PLX^2\cos\alpha}{2}\right)$$

Applying the same methods to section 2 yielded

$$\frac{\partial U_{m,2}}{\partial D_y} = \frac{1}{EI}\int_0^X (M_{0,1}\cdot 0)\,dx = 0$$

By defining $U_{m,3} = \frac{M_s^2}{2k}$ it can be found that

$$\frac{\partial U_{m,3}}{\partial D_y} = -\frac{PLX\cos\alpha}{k}$$

Hence
$$\delta_{y,1} = \frac{1}{EI}\left(\frac{PX^3}{6\tan\alpha} - \frac{PLX^2\cos\alpha}{2}\right) - \frac{PLX\cos\alpha}{k}$$

2.2.2 Structure 2

As illustrated in *Figure 4b*, the second structure is under the same loading condition as structure 1, but only supported on one end and both x and X are protracting from the left-end of the beam.

Therefore
$$M_s = D_yX + PL\cos\alpha$$

$$M_{0,1} = \frac{Px}{\tan\alpha} + D_yx - D_yX - PL\cos\alpha$$

$$M_{0,2} = \frac{Px}{\tan\alpha} - PL\cos\alpha$$

23

Which gives

$$\frac{\partial U_{m,1}}{\partial D_y} = \frac{1}{EI} \int_0^X \left[M_{0,1} \cdot (x - X) \right] dx = \frac{1}{EI} \left(\frac{PX^3}{6 \tan \alpha} + \frac{PLX^2 \cos \alpha}{2} \right)$$

$$\frac{\partial U_{m,2}}{\partial D_y} = \frac{1}{EI} \int_0^X (M_{0,1} \cdot 0) \, dx = 0$$

and

$$\frac{\partial U_{m,3}}{\partial D_y} = \frac{PLX \cos \alpha}{k}$$

Thus

$$\delta_{y,2} = \frac{1}{EI} \left(-\frac{PX^3}{6 \tan \alpha} + \frac{PLX^2 \cos \alpha}{2} \right) + \frac{PLX \cos \alpha}{k}$$

2.2.3 RMS Value

Considering that the structures in their initial position can be plotted with the linear equation of the line

$$y_i(x) = -\frac{x}{\tan \alpha} + L \cos \alpha$$

The deflected beam is thus equal to

$$Y_{1,2}(P, x, X) = y_i(x) + \delta_{y,1,2}(P, X)$$

Whereas y(x) is derived from $x = 0$ through to $x = L \sin \alpha$ in both cases, whilst $X = L \sin \alpha \to 0$ for structure 1 and $X = 0 \to L \sin \alpha$ for the second structure.

Figure 6
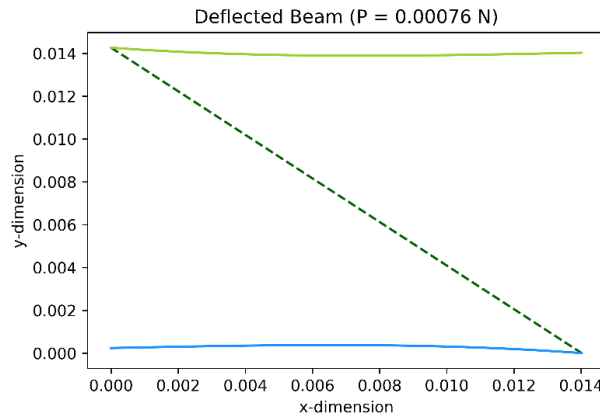*Comparison of the beam models when deformed via the force P = 0.00076 N*

As shown in *Figure 6* the moduli $\left|\delta_{y,1}\right| = \left|\delta_{y,2}\right|$, although the directions of deformation are different due to the variation in the support system. Furthermore, the surface accuracy of the model can be calculated via taking the RMS average of the vertical deflection along the beam relative to the datum line which is equal to $Y_{1,2}(P,x) = \min[Y_{1,2}(P,x)]$ and can be calculated by taking the first derivative of $Y_{1,2}(P,x)$ and substitute the obtained x back into the equation $Y_{1,2}(P,x)$. In order to avoid over-complication and recalling that the RMS value is sign independent (only the magnitudes are important), $\delta_{y,2}$ was preferred over $\delta_{y,1}$ as the former has the same limit as $y_i(x)$. That is, for deflected beam equation of structure 2: $x = X$. The RMS value can therefore be calculated as shown below.

$$RMS(P) = \sqrt{\frac{1}{L\sin\alpha} \int_0^{L\sin\alpha} \{Y_2(P,x) - \min[Y_2(P,x)]\}^2 \; dx}$$

3. Numerical Solutions

In utilising ABAQUS, 4 different models were analysed to numerically obtain the RMS-Tensile Force relationship. Beginning with the 2D beam model, an exact reconstruction of the structure 2 from which the analytical solution was obtained, subsequent models were created in increasing disparity to the simplified problem but closer to reality. These models are the 3D version of a halved single-crease membrane, a full single-crease membrane, and a 3 creases membrane. The latter two, however, were not set up to justify the accuracy of the analytical solution but to investigate the methods to construct a realistic model of the deployable space antenna membranes which invariably include multiple creases.

3.1 Mesh Convergence Study

In order to better establish grounds for physical experiments, the dimensions of the models were objectively small. Subsequently, the range of usable mesh sizes were also limited, the respective largest value for average mesh sizes as shown in *Figure 7a* and *7b* already generated less than 10 meshes throughout the structures. However, considering that the surface accuracy tolerance for a satellite membrane which operates in the Ku-band is ±0.0008 m (i.e. 0.08E-2 m in the unit of the graphs in *Figure 7*) even the largest mesh sizes were technically feasible in terms of result accuracy. However, taking into account that the RMS value is the average of vertical displacements throughout the structures, larger quantity of meshes were preferred as each mesh represents a data point. Ultimately, the average mesh sizes utilised were 1E-4 m^2, 1E-6 m^2, and 6E-6 m^2 for 2D beam model; 3D half single-crease model; 3D full single-crease model and multiple-creases models, respectively. Limitation in computational power meant that the mesh sizes could not be any smaller. It had been recognised that values in ABAQUS are dimensionless and, as such, the models could've been enlarged via working with a smaller system of units [e.g. centimetre(cm) in lieu of metre(m)]. Indeed, the 3D models operated on a cm-based unit system, however, this was essential as the 3D shell elements used to model the structures would not have otherwise been able to capture the required membrane thickness of 50 μm. Consequently, the results obtained would have been

completely inaccurate. On the other hand, the same adjustment was not essential for the 2D models using the ABAQUS beam elements. Additionally, as sufficient data points were available at the previously determined mesh size, standard SI units were maintained for the 2D models to avoid unnecessary complications.
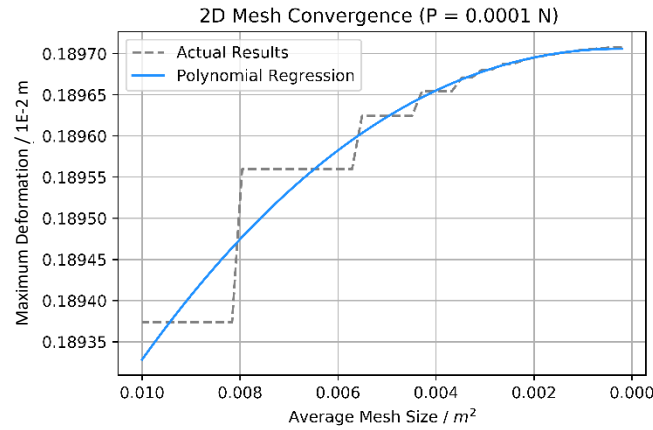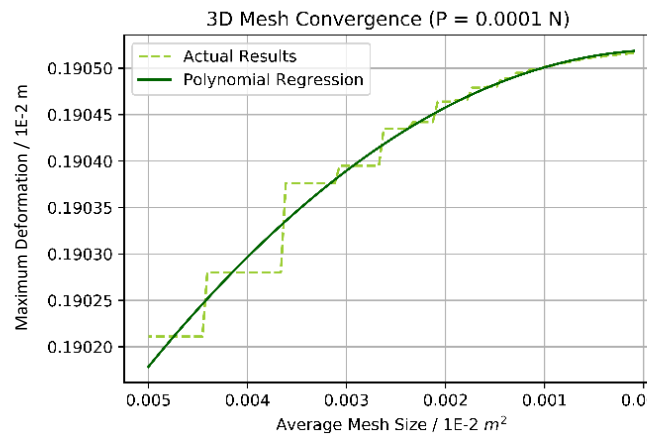
(a) 2D mesh convergence

(b) 3D mesh convergence

Unfortunately, whilst ABAQUS allows raw data to be plotted, it cannot manipulate these data. That is, as the displacement values obtained from an analysis pertain to the movement of data points from their initial positions and not the required vertical displacements from the reference datum lines, the values must be post-processed outside ABAQUS after extraction (see Appendix I). Ergo there are limitations in terms of the employable shapes and distribution of meshes: the meshes must be in the shape of a hexahedron (or quadrilateral for 2D models), and uniformly distributed throughout. The latter is especially important as the location of each data point had to be mapped after being exported from ABAQUS. In comparison, adapting the present algorithm to process data produced from different mesh types poses a less significant challenge. However,

noticing that no changes in accuracy was observable in comparing tetrahedron meshes to hexahedrons used for the 3D model - as shown in *Figure 8*, for instance, the maximum error was less than 1% - there was no justification to modify the algorithm.
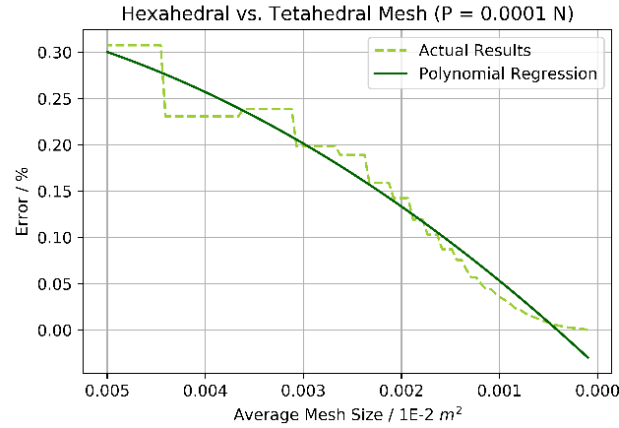

Figure 8 The percentage error in the values of maximum deformation at P = 0.0001 N obtained from models analysed with hexahedral meshes, and tetrahedral meshes at different average mesh sizes.

3.2 Two-dimensional Beam Model

The 2D beam model was generated using the ABAQUS beam elements as shown in *Figure 8*. With the material properties of a 50 μm thick Kapton film as listed in *Table 1*, the model is 0.02 m long. For the analysis, the model was subjected to different conditions in 2 steps. The initial step implemented the boundary conditions following the support system of structure 2 (see *Figure 4b*) which fixed the displacement in the left-end of the model to zero in all directions except for rotation around the z-axis [denoted as degree of freedom (DOF) number 6]. Subsequently, the point load was applied in the second step on the right-end of the model with constant direction towards the positive x-axis direction. As illustrated in *Figure 9*, the crease-induced stiffness implemented using the provided spring "engineering feature" to connect the left-end point to the ground, whereas the spring constant was set to k.

Constant	Value	Unit
E	2.5×10^9	Pa
k	1.2×10^{-5}	N m deg.$^{-1}$
α	44.5	deg.
v	0.34	–

Table 1 Constant Values for ABAQUS Modelling
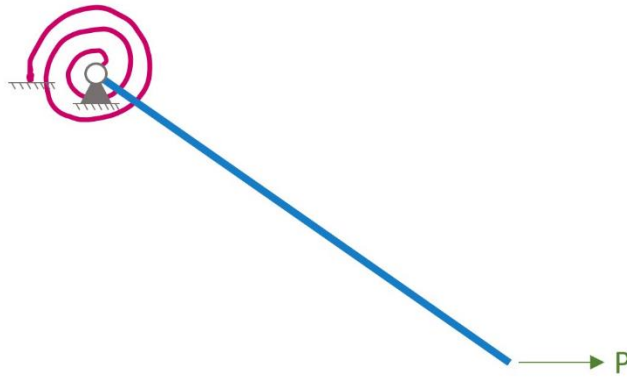
ABAQUS provides the option for the time step to be divided into separate increments, as such this would enable the displacement values in response to multiple different magnitudes of force P to be obtained through a single sequence of analysis. However, whilst the load application could have been set to be linearly distributed in proportion to the cumulative amount of time elapsed as each increment was reached, the size of each time step is neither user-describable nor uniform. Consequently, the magnitude of the load "applied" at each increment would have to be identified individually.

On the contrary, taking advantage of the fact that ABAQUS operates on Python, a script was written utilising the loop function to run the analysis through different P value from 1E-5 N to 0.001 N with the step increase of 1E-5 N (see Appendix II). The script also automated the data, and image extraction at each P value.

3.3 Single-crease Membrane Model

With reference to the material properties and dimensions detailed in the previous section (4.2), the 3D model of a halved single-crease membrane was created with the ABAQUS shell element. Reflecting the beam model, the membrane has the length of 0.02 m and equal width of 0.02 m extruded from a 50 μm thick rectangular cross-section.

The model was also subjected to a zero-displacement boundary conditions in all directions but DOF=6 along the left-edge of the model. However, instead of the point load, the force is applied through a "shell edge load" uniformly distributed along the right-edge of the

model with constant direction as shown in *Figure 10*. The load is defined as $P_d = \frac{P}{b}$ N m^{-1}.

As the spring constraint can only be connected to points and not edges, it was necessary to apply a kinematic coupling constraint onto the entire left-edge of the model to ensure the effect of the torsional spring extended to cover the required region. This kind of coupling constraint eliminates some DOFs at the recipient "coupling" region and instead replace the region's response motion to that of the "control" node. As displayed in *Figure 10*, the control point is where the spring constraint is applied with the spring constant k.
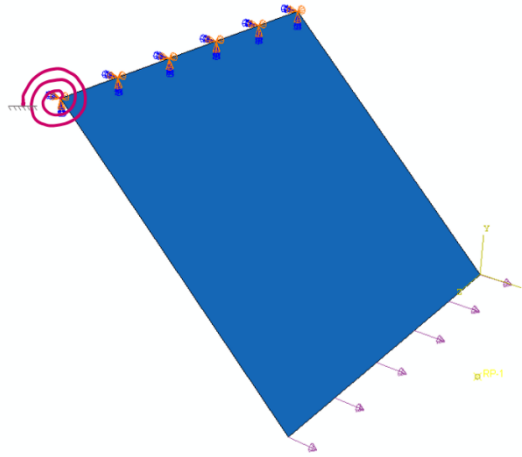

Figure 10 3D halved single-crease model showing the pinned support, uniformly distributed shell edge load, and the spring constraint applied at the control point of coupling the entire right edge.

However, the same adjustment cannot be used to connect two 3D models together to form a full single-crease membrane. Whilst the load was applied using the same technique along the same edge, the displacement constraint which represents the pinned support was moved to the left edge of the second panel as observable from *Figure 11*. Additionally, a roller support was also placed under the right-edge by a displacement constraint in the positive y-axis direction to simulate a more realistic condition in which the right-edge at which the tensile force is acting on would be clamped. Furthermore, in place of the torsional spring, a connector was necessary to relate the responses of the two planes. As per the method originally proposed by Dharmadasa et al.[13] in 2016, the Revolute connector was chosen with the rotational elasticity defined to be equal to the constant k. As opposed to other connectors which align rotating parts, such as Cardan or Rotation, Revolute can only constraint in the rotation around the x-axis (i.e. DOF = 4), thus

a separate coordinate system was required to act as the reference datum. As shown in figure 10, the new cartesian coordinate system has the positive x-axis direction pointing in the negative z-axis direction of the global system.
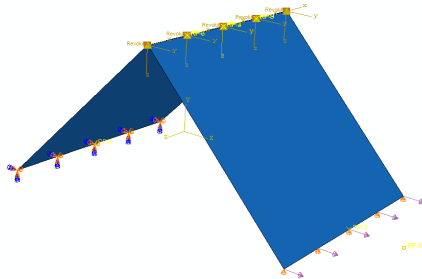
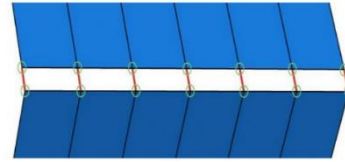

Figure 11 3D single-crease model

Figure 12 Perpendicular wires[13]

The connector was assigned to act on a set of 5 wires, perpendicular to the edges, connecting the two membrane as illustrated in *Figure 12*. Having the wires as one set meant that the value of k did not have to be divided by 5 as the effect is automatically distributed equally. In addition to the connector, however, the Tie constraint was also used to connect the two edges to further ensure that the influence of increased stiffness is transferred across both surfaces. Although the 50 µm space must be left between the two edges (see *Figure 12*) to allow for the presence of the wires, the planes remain close enough for the Tie constraint to remain in effect.

Akin to the loop created for the 2D model, 2 different loops were also created to run through the model creation, analyses, and data extraction at various value of P (see Appendix III).

3.4 Multiple-creases Membrane Model

Building on the methods established previously with respect to the 3D model of a full single-crease membrane, a membrane with 3 creases was constructed as illustrated in *Figure 13* below.

Each plane has the same dimensions of length, width, and thickness as mentioned in the previous sections, with the opening angle of $2\alpha = 89°$. The same constraints and shell-edge load applies at the left- and right-edge of the model, respectively. The 4 planes were all connected at the edge with Revolute connectors, and Tie constraints as described in

section 3.3. Initially the model was analysed without the roller support in the middle section, however, the resulting respond captured was not as expected as it appeared that that the effect of the tensile force was not transferred to the middle two planes (see *Figure 14*). On the other hand, incorporating the roller support produces the response illustrated in *Figure 15*. Nonetheless, since the membrane would be suspended in vacuum unsupported, further investigation has been made in the attempt to construct the model unsupported as discussed in section 5.3.
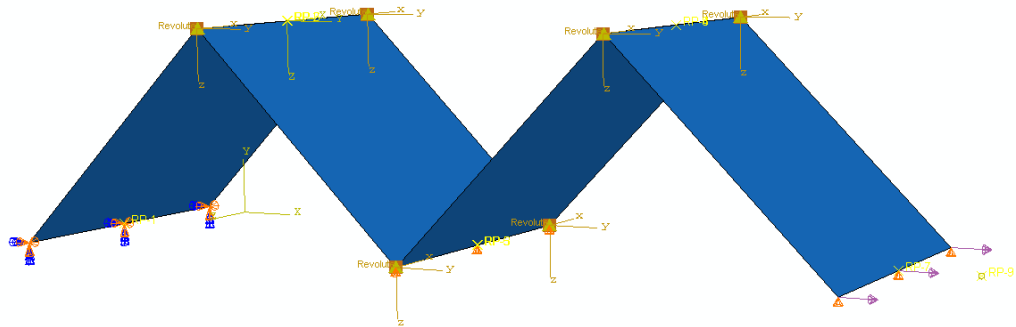

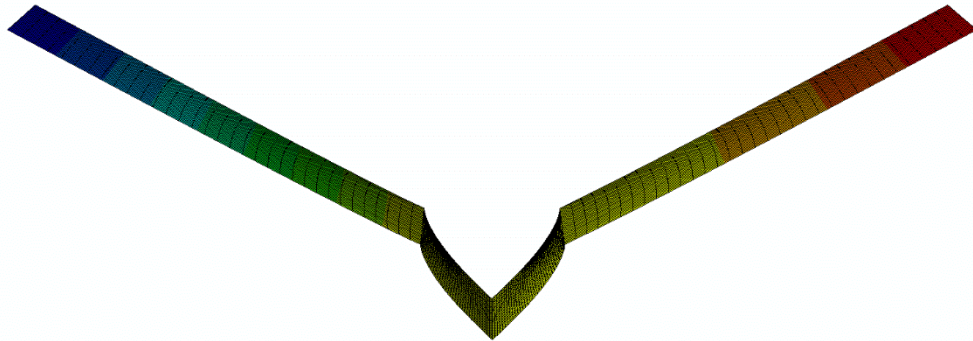*Figure 13 3D 3 creases model*

Figure 14 Response without roller support under the middle crease (P = 0.0007; Deformation Scale Factor = 1)

Figure 15 Response with roller support under the middle crease (P = 0.0007; Deformation Scale Factor = 1)

3.5 Data Processing

After each analysis, the outputs were recorded on a separate .odb file detailing the displacements of each node throughout the structure, amongst other attributes. The displacement values were exported to .txt files and processed via Python on the Jupyter computing environment. Following the meshing criteria aforementioned in section 4.1, the displacement values obtained in the format automatically generated by ABAQUS (see Appendix IV) could easily be mapped to its respective location on the structure. For example, with the average mesh size of 0.0001 m^2 for the 2D model, the displacement value was collected for each of the 20001 nodes present, whereas node no. 1 is located at the pinned-end of the beam, and node no. 20001 is located at the opposite end. This linear relationship is also repeated for the 3D models; however, the nodes must be further divided into sets representing the displacement along the length of the membrane with respect to an infinitesimal amount of width. Considering the simplified topside view of a 3D panel in *Figure 16*, it can be observed that for the first set node no. 1 denotes the displacement at the lower-left corner of the membrane. As such, node n yields the displacement at the upper-left point on the pinned end, whereas the n also represents the number of data points in a set.
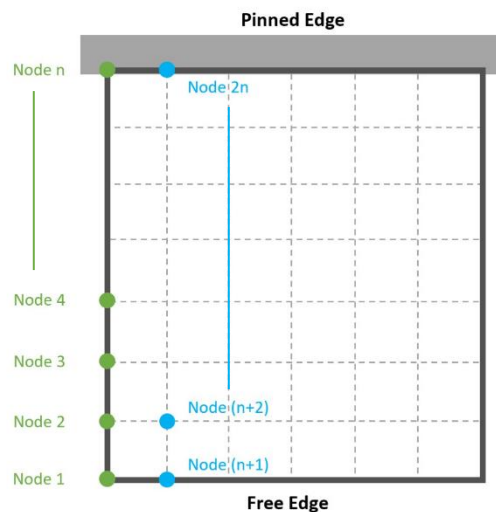

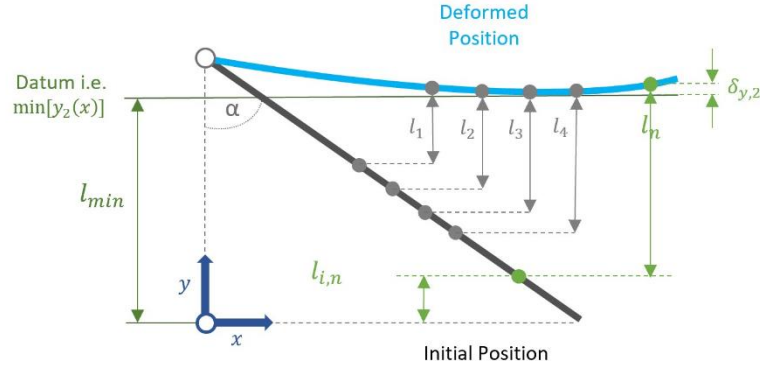*Figure 16 Top-view of a 3D membrane*

Figure 17 Simplified model of a 2D deformed beam

Considering that the mesh size used would be consistent in all analyses of the same model, even with different magnitude for P, the n value is thus constant and could be easily identified manually. Especially considering that each membrane is a square, the n value is thus simply equal to the square root of the total number of nodes. For instance, the 3D half single-crease model has 40401 nodes in total with $n = 201$ nodes in a set, giving 201 sets. For the full single-crease, and 3 creases models, there is 1156 per panel: totaling to 2312 nodes for the former, and 4624 for the latter. Thus, there are 68 sets of 34 nodes for the single-crease model, and 136 sets for multiple-creases model.

Subsequently, the displacement values could be manipulated to yield the required relative vertical deflection as shown in *Figure 17*. That is, l_n is the value obtained through ABAQUS whilst recalling that $\delta_{y,2}$ is the value required. Through mapping the locations of each node, the initial y-coordinate $l_{i,n}$ at node n could be obtained as both the initial length and slanting angle α are known.

Thus,
$$\delta_{y,2} = \left(l_n + l_{i,n}\right) - l_{\min}$$

Where
$$l_{min} = \min[y_2(x)]$$

After having acquired the vertical deflection, it became possible to calculate the numerically obtained RMS value as below.

$$RMS = \sqrt{\left(\frac{\sum_{n=1}^{N} \delta_{y,2,n}}{N}\right)^2}$$

4. Results & Validation

4.1 Viability of 2D Simplification

One of the initial assumptions referred to in this study, arising from the symmetry condition in the cross-section of the membrane in the xy-plane, is the simplification of a 3D problem into a 2D beam model. The function which relates RMS to the tensile force itself (section 2.2.3) was obtained from a 2D problem. To verify the assumption, the RMS values of the numerical models were plotted against their corresponding P value (End Load). Observing *Figure 18a* the two plots align almost perfectly up to the point of minimum RMS (2DRMS) value for the beam model as denoted by the first dashed line from the left, beyond which the lines begin to diverge. The percentage error shown on *Figure 18b* reaches the first peak of 40% at P = 0.00072 N before reaching the highest error at 95.47%, the average error stands at 16.86%. Considering the peak and mean errors alone, it may appear that the 2D simplification is invalid.
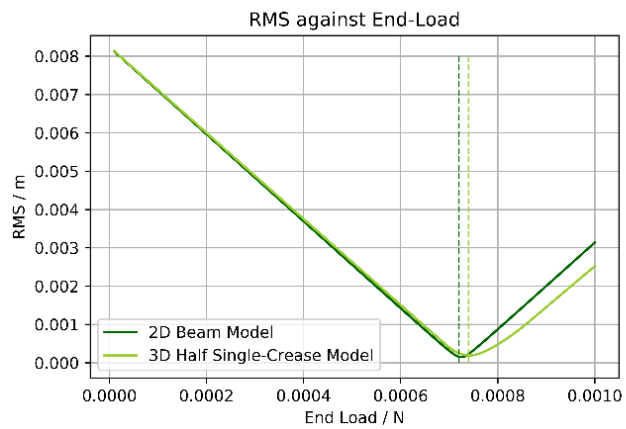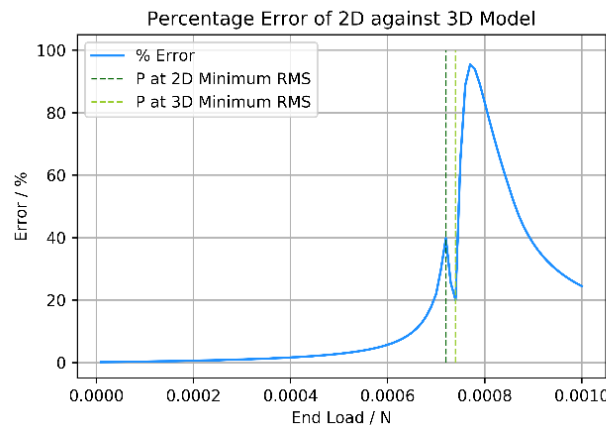

Figure 18
Comparisons of 2D beam model with 3D half single-crease model

(a)

(b)

However, it is important to recall that the purpose which follow the aim of this project to link RMS and the tensile force is to estimate the force required to achieve a flat surface: that is, the 2DRMS. By incorporating a conservative limit to the minimum RMS of the 2D beam model, that is the accuracy of the simplification will not stand beyond this point, the assumption could be proven to be valid. As such, the new mean percentage error where $P \leq 0.00072$ is only 3.36%.

4.2 Validating the Analytical Solution

Further comparison was made between the analytical solution for RMS and the values obtained through the two numerical models representing one half of a single-crease membrane. The peak error was found to be 206.86% and 84.70% for the 2D and 3D model, respectively. Both values occurred at the same moment in which the coincidental end-load is P = 0.00072 N. Similarly, the mean error of the 2D model is higher at 27.37%, whilst the mean error stands at 16.03% for 3D model. Observing *Figure 19a*, it is clear that the analytical solution overestimated the force required to achieve the minimum RMS value. Indubitably, one of the main contributing factors to the error would be the small-deflection limitation of the Castigliano's second theorem that could not produce a singular function to define both the horizontal, and vertical deflection along the beam. Although it would've been possible to also calculate deformations in the x-direction by incorporating a horizontally-facing dummy load, it was impossible to produce a solution for the RMS value without using numerical methods to approximate the answer, thus defeating the aim of this paper. It is not difficult to imagine that the analytical beam would've became flatter with weaker force if it was "allowed" to also extend horizontally as well as vertically.

Despite the assumptions and errors, the analytical method does offer a practical value in terms of achieving the RMS value within the required tolerance, as illustrated by the shaded areas of the graphs below. Considering the scenario in question, for instance, where the optimum end load was calculated to be at P = 0.00077 N; whilst the recorded errors at this point are 77.63% for the 2D model, and 56.28% for the 3D, the RMS values (0.00012 m for 2D and 0.00027 m for 3D) remain below the accepted tolerance of ±0.00083 m.
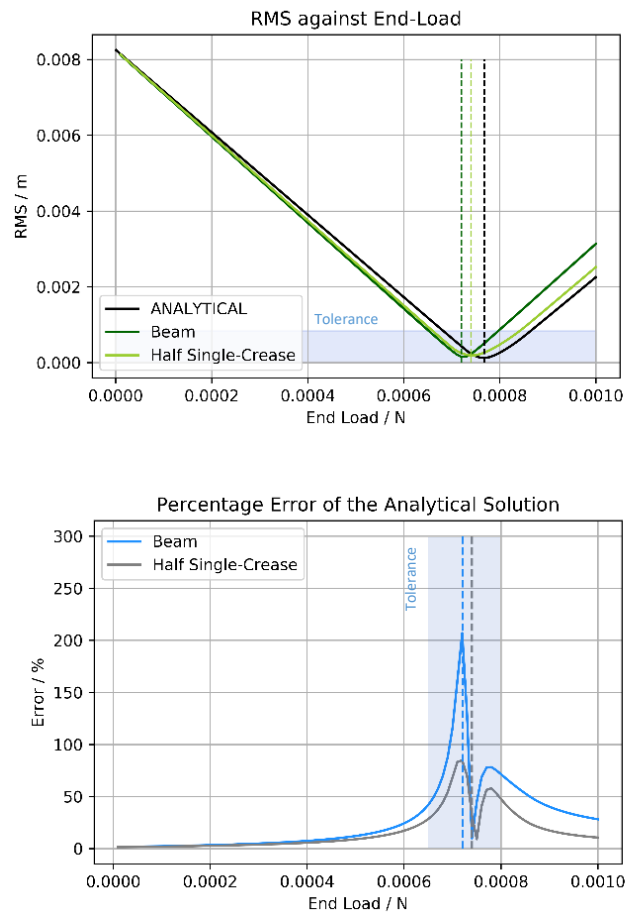
Figure 19 Comparison of the analytical solution to numerically obtained RMS values of 2D and 3D model of one half of a single-crease membrane

Nonetheless, it was recognised that better method must be obtained in light of the fact that the sizes of the models investigated, and by proxy the deflections, were objectively much smaller than a typical antenna. Not to mention that the analyses were conducted under static conditions - that is the systems do not undergo any acceleration with the application of the loads – which will not hold true in reality where the tensile force would be applied within a period of time and that the extension of the membranes will be subjected to acceleration, and thus inertial force presently unaccounted for.

4.3 Modelling Multiple-creases Models

As previously discussed in section 3.4. The method employed to create the single-crease model did not produce the expected solution from the multiple-creases model. Whilst it appeared obvious that the issue lies with the middle section involving two planar membranes, the cause was less clear. Recalling the study which proposed the Revolute & Tie constraint combination, two more methods were also discussed: Perfect Hinge and Perfect Weld.

Whilst there is a connector on ABAQUS named Hinge, the Perfect Hinge in this case refers to the extension of the Tie constraint to also restrict the relative rotational motions and completely fuse together the different parts, instead of the rotational motions being restricted by the Revolute connector. Perfect Weld refers to the Weld connector which combines the effect of the Join and Align connectors, effectively holding the opening angle constant regardless of the tensile force applied. However, whilst the majority of models incorporating these alternative methods could be processed fully, the tensile force required was grossly overestimated with the crease(s) essentially being too "stiff". Additionally, the welded model suffered further from the inaccuracy which arose from the opening angle being kept constant.

For this additional analysis, the modelling process was retracted back to the 2D stage in the attempt to better understand the different combination of constraints and connectors in ABAQUS. Strictly modelling on the xy-plane, however, meant that connectors which requires the z-axis were not accepted by ABAQUS, this includes the Revolute connector, Cardan, and also the Hinge connector. Recalling that the Hinge connector is equivalent to applying Join and Revolute. Connecting the different parts with a Spring, either on its own or in combination with the Tie constraint (without rotational restriction), were possible but failed to produce a processible model. Consequently, the model could only be run either under Tie constrain, or when welded together. The methods, however, as discussed previously produced inaccurate results. Additionally, even if the error in the stiffness of the crease is neglected, when the methods were used on a 2D model with 3 creases, the issue reappeared in which the middle section did not deform as expected.

Hence, specifically with regards to modelling multiple creases models in the future, it is urged that the focus be placed on resolving the issue on a 3D model.

5. Conclusion and Future Work

This study has been conducted to achieve two main goals. Firstly, to define the tensile load-surface accuracy relationship of a creased-membrane for aiding the design of deployable space antenna. Secondly, to explore the methods to model a membrane with multiple creases on the FEA software ABAQUS.

With regards to the first aim, the equation which defines RMS – the measure of surface accuracy – as a function of the tensile force (P) was formed using the Castigliano's second theorem on displacement and strain energy of a beam to analyse a 2D beam model. On the basis that the membrane's length (L), neutral angle (α), second moment of inertia (I), and the material's Young's modulus (E) are known and can be treated as constants. The function was validated by comparing its RMS values to the equivalent values obtained through numerical analysis of 2 models created on ABAQUS with the same specifications, whereas the percentage errors have the mean average of 27.37% and 16.03% for the 2D, and 3D model, respectively. Further considering the surface accuracy tolerance of an antenna which operates in the Ku-band – widely used in communications on space shuttles, as well as for satellite televisions – it was found that the optimum end-load magnitude proposed by the function produce the numerical RMS within the tolerance. Thus, the function was considered validated within the scope of practicality. However, as the Castigliano's theorem is only accurate for small deflections, future work will be required in deriving the relationship using the elastica theory for large deflection. Additionally, both the analytical solution and the numerical models can be further validated through an experimentation, for which all reference dimensions used in this paper were predetermined. Nevertheless, the function provides a relatively quick and simple method in estimating the force required to achieve the desired RMS value, which should assist future designs in both the material selection, and tensioning mechanism design process.

On another note, although not the main objective, the same models were also used to verify the 2D simplification, in which the percentage disparity of the reference values was found to have the mean average of 3.36% within the relevant range of the load magnitude. Minor limitation was encountered with regards to the computational power

of the available facilities, however, any inaccuracy arising from this reason was negligible as described earlier in this paper.

Concerning the second aim, the 3D model of a full single-crease membrane was generated and produced the expected results. However, attempts to utilise a similar method to form a membrane with three creases were unsuccessful, with the apparent issue being the analysis' failure to induce a mechanical response in the middle sections. Nonetheless, this paper details a clear explanation of the three methods conventionally used to model a creased-membrane: Perfect Hinge, Perfect Weld, and the Revolute-Tie constraint combination. Furthermore, concluding from the results of some further attempts at diagnosing the issue undertaken for this paper, future effort is recommended to be directed at modelling the crease in 3D only as the single-crease model was successfully modeled for this project with acceptably accurate results. Ultimately, considering the lack of published studies within this specific area of study, it is also advisable to consult the ABAQUS developer's manual for information on the specific connectors and constraints.

BLANK PAGE

References

1. Tibert, G. (2002). Deployable Tensegrity Structures for Space Applications. Royal Institute of Technology.

2. Russell, R., Campbell, T. and Freeland, R. (1980). NASA Technology for Large Space Antenna. NASA Langley Research Centre.

3. Canadian Space Agency. (2018). Satellite characteristics. [online] Available at: http://www.asccsa.gc.ca/eng/satellites/radarsat/radarsat-tableau.asp [Accessed 29 Sep. 2018].

4. Lee, N. and Pellegrino, S. (2014). Multi-Layered Membrane Structures with Curved Creases for Smooth Packaging and Deployment. American Institute of Aeronautics and Astronautics.

5. Leipold, M., Runge, H. and Sickinger, C. (2005). Large SAR Membrane Antennas with Lightweight Deployable Booms. ESA/ESTEC.

6. Wang, C., Tan, H. and He, X. (2011). Wrinkle-crease Interaction Behaviour Simulation of a Rectangular Membrane under Shearing. The Chinese Society of Theoretical and Applied Mechanics and Springer-Verlag Berlin Heidelberg.

7. Xiao, W., Chen, W. and Fu, G. (2011). Wrinkle Analysis of the Space Inflatable Paraboloid Antenna. Shanghai Jiao Tong University.

8. Lechenault, F., Thiria, B., Adda-Bedia, M. (2014). Mechanical Response of a Creased Sheet. American Physical Society.

9. Papa, A., Pellegrino, S. (2008). Systematically Creased Thin-Film Membrane Structures. University of Cambridge.

10. Mutyalarao, M., Bharathi, D., Nageswara Rao, B. (2010). Large Deflections of a Cantilever Beam Under an Inclined End Load. Andhra University.

11. Dharmadasa, B., Mallikarachchi, H., Jimenez., F. (2018). Characterizing the Mechanics of Fold-lines in Thin Kapton Membranes. American Institute of Aeronautics and Astronautics.

12. Liu, Z., Qiu, H., Li, X. and Yang, S. (2017). Review of Large Spacecraft Deployable Membrane Antenna Structures. Beijing Institute of Spacecraft System Engineering.

13. Dharmadasa, B., Mallikarachchi, H. (2016). Finite Element Simulation of Thin Folded Membranes. University of Moratuwa.

Additional bibliography

1. Ahmed, S. (1980). Structural Requirements and Constraints of High Gain Satellite Antennas for 30/20 GHz Communications. Communications Research Centre.

2. DNAinfo Chicago. (2018). Air and Water Show All Set for Your Instagrams, Texts, Calls and More. [online] Available at: https://www.dnainfo.com/chicago/20140811/lincoln-park/whats-that-on-lake-shore-drive-biggest-baddest-data-tower-around/ [Accessed 25 Sep. 2018].

3. Elektor. (2018). Novel Phased-Array Antenna is an Order of Magnitude Better than Alternative Solutions. [online] Available at: https://www.elektormagazine.com/news/novel-phasedarray-antenna-is-an-order-of-magnitude-better-than-alternative-solutions [Accessed 25 Sep. 2018].

4. Ferland, E. (2005). Analysis and Design of a Synthetic Aperture Radar Membrane Antenna. McGill University.

5. Huang, J. (n.d.). Spacecraft Antenna Research and Development Activities Aimed at Future Missions. pp.485-536.

6. Investigation of Geometric Imperfection in Inflatable Aerospace Structures. (2018). Journal of Aerospace Engineering, 17(3), pp.98-105.

7. MacNeal, R. and Robbins, W. (1966). Tensile Properties of a Tape with a Transverse Crease. Astro Research Corporation, pp.1-14.

8. Mangenot, C. (2008). Antenna : Needs and Technologies.

9. Sabbadini, M. (n.d.). Antenna design for Space Applications.

10. Séguin, G., Pellerin, T., Colinas, J., Baylis, A., Audet, N., Camelo, L., Wood., P. (2002). Membrane Antenna for SAR Satellite. Canadian Space Agency.

11. Phys.org. (2018). SMAP satellite extends 5-meter reflector boom. [online] Available at: https://phys.org/news/2015-02-smap-satellite-meter-reflector-boom.html [Accessed 25 Sep. 2018].

12. Straubel, M., Langlois, S., Sinapius, M. (2010). Very Lage Stable Membrane Antenna Architectures. German Aerospace Centre.

Appendices

All codes and data developed/obtained for this project are publicly accessible on Github at https://github.com/Joe2303/MECH0020_AS/.

Below is the list of what can be expected from the online repository in relations to the content of this report.

It must be noted that all the codes provided have been adapted to the .py Python code format but originally written in the .ipynb file extension and operated in the Jupyter Notebook environment.

Appendix I: Python Codes for Post-processing

Including the RMS values and graphs generation, and the mesh convergence analysis.

Appendix II: Python codes for the 2D beam model on ABAQUS

Including the code which loops the model through a range of end-load magnitudes, as well as its variant utilised to identify mesh convergence.

Appendix III: Python Codes for 3D models on ABAQUS

Including the code which loops different 3D models through a range of end-load magnitudes, including the half single-crease model, full single-crease models and the multiple-creases model with a roller support in the middle crease.

Additionally, in this section is a variant of the half single-crease model used for the 3D mesh convergence study.

Appendix IV: Numerical results in .txt files, and images in .tiff.

An accumulation of all raw data obtained through ABAQUS.